Enhancing ion transport in charged block copolymers by stabilizing low symmetry morphology: Electrostatic control of interfaces

Jaemin Min[a], Ha Young Jung[a], Seungwon Jeong[a], Byeongdu Lee[b], Chang Yun Son[a,1], and Moon Jeong Park[a,1]

[a]Department of Chemistry, Division of Advanced Materials Science, Pohang University of Science and Technology, Pohang 790-784, Korea; and [b]Advanced Photon Source, Argonne National Laboratory, Argonne, IL 60439

Edited by Frank S. Bates, University of Minnesota, Minneapolis, MN, and approved June 24, 2021 (received for review April 28, 2021)

Recently, the interest in charged polymers has been rapidly growing due to their uses in energy storage and transfer devices. Yet, polymer electrolyte-based devices are not on the immediate horizon because of the low ionic conductivity. In the present study, we developed a methodology to enhance the ionic conductivity of charged block copolymers comprising ionic liquids through the electrostatic control of the interfacial layers. Unprecedented reentrant phase transitions between lamellar and A15 structures were seen, which cannot be explained by well-established thermodynamic factors. X-ray scattering experiments and molecular dynamics simulations revealed the formation of fascinating, thin ionic shell layers composed of ionic complexes. The ionic liquid cations of these complexes predominantly presented near the micellar interfaces if they had strong binding affinity with the charged polymer chains. Therefore, the interfacial properties and concentration fluctuations of the A15 structures were crucially dependent on the type of tethered acid groups in the polymers. Overall, the stabilization energies of the A15 structures were greater when enriched, attractive electrostatic interactions were present at the micellar interfaces. Contrary to the conventional wisdom that block copolymer interfaces act as "dead zone" to significantly deteriorate ion transport, this study establishes a prospective avenue for advanced polymer electrolyte having tailor-made interfaces.

charged block copolymers | ionic conductivity | low symmetry morphology | interfaces | electrostatic interactions

Block copolymers have attracted extensive attention over the past decades owing to their fascinating self-assembly into nanoscale, periodic structures (1, 2). Due to past industrial demands for polymer processing, early studies on block copolymers focused on the modulation of their rheological properties through the incorporation of selective or neutral solvents (3, 4). Such steadfast research efforts on block copolymer thermodynamics, with and without additives, have established the Flory–Huggins interaction parameter (χ) and the block volume fraction (f), which are universal factors used to determine phase diagrams (1, 5–7).

Variable χ values of functionalized block copolymers were found to yield high-fidelity, nanoscale morphologies (8, 9). This was noted to promote advances in the controlled synthesis of block copolymers tethered with functional moieties (10, 11), specifically, the facile tuning of nanostructures (12, 13) and even the creation of hierarchical morphologies (14). The diverse functionality of tailor-made block copolymers enables their use in various applications, such as magnetic storage devices (15), nanoporous membranes (16), and nano-optics technologies (17). Particularly, the covalent and physical incorporation of ions into block copolymers has greatly reduced potential safety threats of energy storage and transfer devices (18, 19). Therefore, in recent years, this has emerged as a fundamental and imperative technology for developing electrochemical and electromechanical systems (20, 21).

Notably, recent experimental (22–24) and theoretical studies (25–28) have revealed unique self-assembly behaviors of charged block copolymers. Examples of this include a series of experimental work of Park et al. (13, 24, 29–32) and theoretical investigation of Olvera de la Cruz et al. (26–28). These works demonstrated that if electrostatic interactions existed in one of the blocks, the phase boundaries between ordered morphologies radically shifted. Accordingly, even with minor ionic blocks ($f_{\text{ionic block}} < 0.5$), hexagonally packed cylindrical (HEX) structures with ionic matrices were formed (26, 29). The strength of the long-range interactions within these ionic blocks played a crucial role in modifying chain stretching and interfacial curvatures.

Moreover, Park and coworkers have unveiled remarkably rich, three-dimensional morphologies, such as face-centered cubic (FCC), bicontinuous gyroid, and orthorhombic *Fddd*, from charged block copolymers through the fine control of intermolecular interactions (13, 31). These are noteworthy in two respects. First, although network morphologies are desirable for advanced polymer electrolytes with efficient ion conduction, they have not been easy to access, especially in the presence of electrostatic interactions. Second, all of the aforementioned morphologies possess major ionic phases, which greatly contribute to improving the ionic conductivity of block copolymer electrolytes. These are the first investigations seeking to boost the ion transport efficiency of block

Significance

We show the enhancement of ion transport properties for charged block copolymers comprising nonstoichiometric ionic liquids by stabilizing the cubic Frank–Kasper A15 phases. The ionic liquid cations predominantly present near the micellar interfaces to increase stabilization energies of the A15 structures if they have strong attractive electrostatic interactions with the charged polymer chains. Unprecedented reentrant phase transitions between lamellar and A15 structures occur through the electrostatic control of interfaces, resulting in radical changes in the conductivity by an order of magnitude. This study is one of the rare demonstrations of a low symmetry morphology to establish a prospective avenue for advanced polymer electrolytes having tailor-made interfaces. Our findings will have implications for energy storage and transfer devices.

Author contributions: M.J.P. designed research; J.M., S.J., and C.Y.S. performed research; B.L. contributed new reagents/analytic tools; J.M., H.Y.J., S.J., B.L., and M.J.P. analyzed data; and J.M., C.Y.S., and M.J.P. wrote the paper.

The authors declare no competing interest.

This article is a PNAS Direct Submission.

[1]To whom correspondence may be addressed. Email: moonpark@postech.ac.kr or changyunson@postech.ac.kr.

This article contains supporting information online at https://www.pnas.org/lookup/suppl/doi:10.1073/pnas.2107987118/-/DCSupplemental.

Published August 3, 2021.

copolymer electrolytes, which namely focused on establishing thermodynamics and a morphology–transport relationship.

Recent discoveries of topologically close-packed phases from a few block copolymers with high conformational asymmetry opened a new forum for polymer science, as implicated by Shi et al. (33, 34), Bates et al. (35–37), and Mahanthappa et al. (37). To introduce interfacial curvature into low symmetry morphologies, a universally applied approach includes varying the chemical structures of the repeating units of the block copolymers to ensure they have largely dissimilar statistical segment lengths (38, 39). Even though the stability window of such morphologies is known to be very narrow, block copolymer/homopolymer blends (40–42), asymmetric block copolymer/symmetric block copolymer blends (43, 44), and block oligomer/water mixtures (45) have been recently found to exhibit Frank–Kasper phases and fascinating phase transitions among them.

Nevertheless, examples of low symmetry morphologies constructed from charged block copolymers remain scarce; therefore, the mechanism for stabilizing such polymorphs with prevailing long-range intermolecular interactions is unknown. Here, we report the stabilization of A15 structure, a type of the Frank–Kasper phases, of charged block copolymers through the control of electrostatic interactions. A methodology that enables prediction and easy access of A15 phases for charged block copolymers was established, which has not been reported in the literature on polymer electrolytes. By combining X-ray scattering experiments and molecular dynamics (MD) simulations, it was revealed that interfacial charge distribution and fluctuation played a key role in stabilizing the A15 structures of the charged block copolymers. Furthermore, when comparing the A15-forming samples with their lamellar-forming counterparts, the ionic conductivity of the former was found to be greater than that of the latter by one order of magnitude.

Results and Discussion

Electrostatic Control of Block Copolymer Morphology. To electrostatically control the morphology of charged block copolymers, two strategies were sought: 1) one set of acid-tethered block copolymers having different types of acid groups was synthesized to control the ionization strengths of the polymer matrices, and 2) nonstoichiometric ionic liquids were incorporated into the polymers to modulate the electrostatic interactions. Dissimilar acid functional groups of sulfonic acid and sulfonyl(trifluoromethanesulfonyl) imide were introduced into polystyrene (PS) chains of a PS-*b*-PMB (PMB: polymethylbutylene) precursor block copolymer via postmodification routes. The PS-*b*-PMB precursor has a nominally symmetric molecular weight of 1.1-*b*-1.2 kg · mol^{-1} with a PS block volume fraction (f_{PS}) of 0.43. The PS units of PS-*b*-PMB first underwent random sulfonation reactions, which gave a PSS-*b*-PMB (PSS: poly(4-styrenesulfonate)) block copolymer with a modification degree of 35 mol.%. Some of the synthesized PSS-*b*-PMB compound was then used in subsequent chemical modifications to yield a PSTFSI-*b*-PMB (PSTFSI: poly(4-styrenesulfonyl(trifluoromethanesulfonyl) imide)) block copolymer (*SI Appendix*, Figs. S1 and S2) (46). Therefore, these two block copolymers (PSS-*b*-PMB and PSTFSI-*b*-PMB) possess the same degree of polymerization, identical molecular weight distributions, and equivalent chain sequence, but they have different types of tethered acid groups ($-SO_3H$ and $-SO_2NHSO_2CF_3$). The volume fractions of PSTFSI (f_{PSTFSI}) and PSS (f_{PSS}) in PSTFSI-*b*-PMB and PSS-*b*-PMB were calculated to be 0.50 and 0.45, respectively, based on the densities of the constituents.

While the PS-*b*-PMB precursor showed disordered morphology, the attachment of acid functional groups gave well-defined gyroid and lamellar (LAM) structures for PSTFSI-*b*-PMB and PSS-*b*-PMB, respectively. Representative small-angle X-ray scattering (SAXS) profiles of the neat block copolymers are shown in *SI Appendix*, Fig. S3. The domain size of PSTFSI-*b*-PMB was ~20% larger than that of PSS-*b*-PMB, attributed to the bulky nature of its $-SO_2NHSO_2CF_3$ (TFSI) moiety. Nonstoichiometric ionic liquids comprising 2-ethyl-4-methylimidazole (2E4MIm) and bis(trifluoromethane)sulfonimide (HTFSI) were introduced into the PSTFSI-*b*-PMB and PSS-*b*-PMB block copolymers. The list of samples is summarized in Table 1. Upon varying the amounts and molar ratios of 2E4MIm/HTFSI, we aimed to modulate the balance of attractive and repulsive interactions of charged polymer chains with $2E4MIm^+$ cations and $TFSI^-$ anions, respectively.

Fig. 1 *A* and *B* show the phase diagrams of PSTFSI-*b*-PMB and PSS-*b*-PMB, respectively, containing the ionic liquids, as determined by SAXS measurements. As shown in Fig. 1*A*, PSTFSI-*b*-PMB presented morphological changes from a gyroid structure to a LAM structure upon the addition of 30 weight (wt)% 2E4MIm/HTFSI (1/1), which also resulted in an increase in domain size from 7.9 to 9.1 nm. The LAM structure was further transformed into HEX phases at a fixed ionic liquid content of 30 wt% but with increased 2E4MIm/HTFSI ratios of 2/1 and 3/1. An analogous LAM-to-HEX transition was also seen when the mass fraction of 2E4MIm/HTFSI (1/1) was increased to 32 wt%. These transitions could be attributed to slight increases in the $f_{PSTFSI} + f_{2E4MIm} + f_{HTFSI}$ values.

Upon further increasing the mass fraction of 2E4MIm/HTFSI to 50 wt%, equilibrium A15 structures were obtained at 2E4MIm/HTFSI ratios of 2/1 and 3/1 via the coexistence of HEX phases and A15 structures at intermediate ionic liquid contents. Except for the noteworthy observation where the A15 structure appeared over a wide phase window, the overall phase behavior of PSTFSI-*b*-PMB comprising 2E4MIm/HTFSI resembles that of block copolymer/selective solvent mixtures in that sequential LAM-to-cylinder-to-sphere phase transitions occurred with increasing volume fraction of ionic phases.

The PSS-*b*-PMB samples exhibited greatly different phase behavior from that of the PSTFSI-*b*-PMB analogs, as they demonstrated a weak dependence on $f_{PSS} + f_{2E4MIm} + f_{HTFSI}$ (Fig. 1*B*). Unprecedented "re-entrance" phase sequences of LAM-to-HEX-to-LAM and LAM-to-A15-to-LAM were observed with increasing $f_{PSS} + f_{2E4MIm} + f_{HTFSI}$. Notably, it took only a small change in the volume fraction of ionic phases to cause the radical morphological transition from LAM to A15. Furthermore, the LAM phases reemerged despite the mass fraction of 2E4MIm/HTFSI increasing from 42 wt% (2/1) to 53 wt% (1/1).

This prompted us to closely examine a set of PSS-*b*-PMB samples loaded with a fixed mass fraction (50 wt%) of 2E4MIm/HTFSI with different molar ratios (Table 1). A15 structures were observed at an $f_{PSS} + f_{2E4MIm} + f_{HTFSI}$ value of 0.71 and 2E4MIm/HTFSI ratios of 2/1 and 3/1 over a wide temperature window of 30 to 150 °C. On the other hand, LAM structures were seen at an $f_{PSS} + f_{2E4MIm} + f_{HTFSI}$ value of 0.70 and a 2E4MIm/HTFSI ratio of 1/1. We thus delineated the phase diagram of PSS-*b*-PMB based on the molar ratio of 2E4MIm to the acid moieties present in polymer and in 2E4MIm/HTFSI ($-SO_3H$+HTFSI), as presented in Fig. 1*C*. The morphology appeared to be remarkably sensitive to the 2E4MIm/($-SO_3H$+HTFSI) ratio, where A15 phases were formed by increasing the amount of 2E4MIm. In contrast, the *x*-axis conversion of the phase diagram of PSTFSI-*b*-PMB showed little dependency on the 2E4MIm/($-NH(SO_2)_2CF_3$+HTFSI) ratios. (*SI Appendix*, Fig. S4).

In the PSS chains, the $2E4MIm^+$ cations are expected to pair with the $-SO_3^-$ anionic moieties over the $TFSI^-$ species owing to the binding affinity between $2E4MIm^+$ and $-SO_3^-$ being stronger than that between $2E4MIm^+$ and $TFSI^-$ (24). This is also because HTFSI is not present in excess for PSS-*b*-PMB samples, leading to deprotonation of $-SO_3H$ groups in PSS chains ($pK_a = -2.1$) in contact with 2E4MIm ($pK_a = 8.7$) to form the

Table 1. PSTFSI-*b*-PMB and PSS-*b*-PMB samples comprising ionic liquids

Polymer	Molar ratio of 2E4MIm/HTFSI/acid group of polymer	Total mass fraction of 2E4MIm+HTFSI (wt%)	Volume fraction of ionic phase (f_{PSTFSI} + f_{2E4MIm} + f_{HTFSI} or f_{PSS} + f_{2E4MIm} + f_{HTFSI})	Morphology
PSTFSI-*b*-PMB	Neat polymer	0	0.50	GYR-GYR/LAM
	0.9/0.9/1.0	30	0.64	LAM–DIS
	1.4/0.7/1.0	30	0.64	HEX
	1.8/0.6/1.0	30	0.65	HEX
	1.0/1.0/1.0	32	0.65	HEX
	2.0/1.0/1.0	38	0.68	A15/HEX–HEX
	3.0/2.0/1.0	52	0.75	A15–DIS
	2.0/2.0/1.0	50	0.73	A15/HEX
	3.3/1.7/1.0	50	0.74	A15
	3.9/1.3/1.0	50	0.75	A15
PSS-*b*-PMB	Neat polymer	0	0.45	LAM–DIS
	0.8/0.8/1.0	30	0.60	LAM–DIS
	1.2/0.6/1.0	30	0.60	HEX
	1.5/0.5/1.0	30	0.61	HEX
	1.0/1.0/1.0	36	0.63	LAM–DIS
	2.0/1.0/1.0	42	0.66	A15/HEX
	2.0/2.0/1.0	53	0.72	LAM–DIS
	3.0/2.0/1.0	56	0.74	A15
	1.8/1.8/1.0	50	0.70	LAM–DIS
	2.8/1.4/1.0	50	0.71	A15
	3.3/1.1/1.0	50	0.71	A15

ionic pair. Density functional theory calculations further support the deprotonation of sulfonic acid group when interacting with 2E4MIm (*SI Appendix*, Fig. S5). Therefore, the increased 2E4MIm content causes an increase in the charging of the PSS chains, which enhances the segregation strength of PSS-*b*-PMB. On the contrary, given that HTFSI is a superacid ($pK_a = -10$), PSS chains could not be preferentially deprotonated if the HTFSI content is increased. This was connected to the formation of the weakly segregated LAM structures, which readily disordered as the temperature increased. In the case of PSTFSI-*b*-PMB, the same conclusion does not apply because the tethered HTFSI of polymer chains and the embedded HTFSI in ionic liquids are similar, and thus, the binding affinity is no more a driving force that attracts $2E4MIm^+$ cations to the $PSTFSI^-$ ionic chains. Therefore, $2E4MIm^+$ cations are expected to spread over the entire ionic phases of PSTFSI-*b*-PMB samples. The charge delocalization of the $TFSI^-$ anions also attenuates the repulsive interactions in the PSTFSI domains, making the morphology less sensitive to the 2E4MIm/HTFSI ratio.

This assessment was supported by extensive MD simulations utilizing state-of-the-art first principles force field developed for the ionic liquids and polymer mixtures (47, 48). The simulations show that thin ionic shell layers surround the PMB core, which is composed of charged PSS^- (or $PSTFSI^-$) and $2E4MIm^+$ complexes. Fig. 1*D* illustrates a representative micellar structure for PSS-*b*-PMB dissolved in 2E4MIm/HTFSI (1/1), as constructed by the simulation. Interestingly, while the stretching of the PMB chains in the micellar core (in ball and stick representation) was apparent, the charged PSS chains (represented with large spheres) were more collapsed. This conformational asymmetry originates from the amphiphilic nature of the randomly sulfonated PSS chains. As illustrated in *SI Appendix*, Fig. S6, the uncharged PS units in the PSS chains show a strong tendency to lie on the micellar interface while pushing the charged PSS units toward the ionic corona.

Fig. 1*E* illuminates the radial distribution of each species for PSS-*b*-PMB and PSTFSI-*b*-PMB micelles in 2E4MIm/HTFSI (1/1). It is noteworthy that tightly bound $2E4MIm^+$ cations were found near the micellar interfaces in the case of PSS-*b*-PMB (strong binding affinity), while the PSTFSI shells were relatively wider for PSTFSI-*b*-PMB (weak binding) and did not present any enhancement of $2E4MIm^+$ cations at the interfacial region. The formation of more diffusive interface with concentration fluctuations is thus predicted for the PSTFSI-*b*-PMB samples. As will be discussed later, both the conformational asymmetry and the cation concentration fluctuation played crucial roles in determining the stability of the A15 phases.

Slow Reenactment of A15 Phases from HEX Structures via an Epitaxial Route. We observed the coexistence of A15 and HEX structures for both the PSTFSI-*b*-PMB and PSS-*b*-PMB samples comprising 2E4MIm/HTFSI (2/1) with mass fractions of 40 ± 2 wt.%, where heating the samples stabilized the HEX structures over the A15 phases. Representative SAXS data obtained for PSTFSI-*b*-PMB are plotted in Fig. 2*A*. As can be seen from the figure, cooling the sample from 130 °C down to room temperature at a rate of 0.5 °C/min did not lead to the immediate reemergence of A15 phases, and the HEX structures persisted. Upon monitoring the morphology of the cooled sample at room temperature for 15 mo, we noted that the extremely slow reenactment of the A15 structures occurred via the d_{211} of the A15 coinciding with the d_{10} of the HEX phases. We surmise that the energy levels of the A15 and HEX phases that formed with a 2E4MIm/HTFSI ratio of 2/1 are essentially degenerate.

Although some portions of the phase diagrams of the PSTFSI-*b*-PMB and PSS-*b*-PMB samples are marked as the A15 and HEX structures coexisting in the same way, there was a difference in the relative fractions of these structures in the samples; specifically, the A15 structure exists to greater degree in the PSS-*b*-PMB sample than in the PSTFSI-*b*-PMB sample. As presented in Fig. 2*B*, while the heating of PSS-*b*-PMB stabilized the HEX phases, cooling the samples from 130 °C to room temperature led to the relatively faster reemergence of the A15 phases. An additional 8 mo of monitoring at room temperature led to the development of well-defined A15 phases that coexisted with a small fraction of HEX structures (inverted triangles). This coexistence may be a consequence of the ternary components of our samples, but the metastable phases of our samples would be easily trapped by a charged medium.

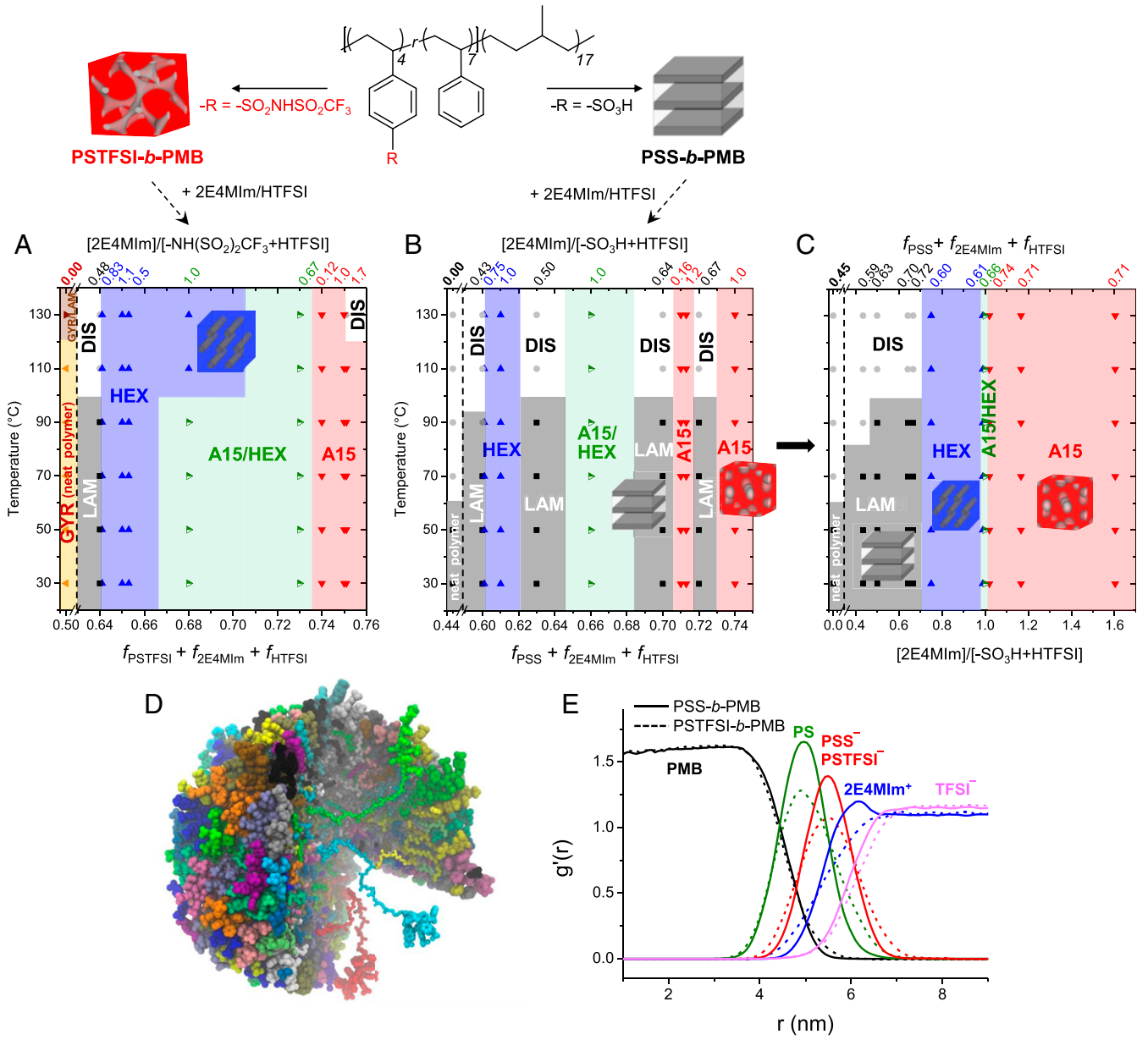

Fig. 1. Phase diagrams of (*A*) PSTFSI-*b*-PMB and (*B*) PSS-*b*-PMB block copolymers comprising nonstoichiometric 2E4MIm/HTFSI ionic liquids as a function of the molar ratio of 2E4MIm to acid moieties as *x*-axis on the *Top* and the volume fraction of ionic phases as *x*-axis on the *Bottom*. (*C*) Phase diagram of PSS-*b*-PMB samples with the $f_{PSS} + f_{2E4MIm} + f_{HTFSI}$ as *x*-axis on the *Top* and the molar ratio of 2E4MIm to acid moieties as *x*-axis on the *Bottom*. (*D*) Representative MD simulation snapshot of a PSS-*b*-PMB micelle dissolved in 2E4MIm/HTFSI (1/1). Each polymer chain is represented with a different color, where the randomly sulfonated PSS chains are drawn as larger spheres and the PMB are shown in ball and sticks. Part of the chains are removed to highlight the conformation of each polymer chain. (*E*) Radial distribution of each species from the center of the PMB core, highlighting dissimilar $2E4MIm^+$ distributions near the micellar interface for PSS-*b*-PMB and PSTFSI-*b*-PMB in 2E4MIm/HTFSI (1/1).

The cylinder-to-sphere transition kinetics are influenced by the interfacial tension of the micelles. In the present study, two interfaces exist at the PMB core/PS interlayer and PS interlayer/ionic corona, as envisaged by MD simulations. For PSS-*b*-PMB samples, with the thin $PSS^-/2E4MIm^+$ layer that formed near PMB/PS interfaces, the resultant PS/PSS^- interface was sharp with high interfacial tension (see Fig. 1*E*) to increase stability window of spherical micelles. Furthermore, contrary to most literature on the phase behavior of block copolymer melts and solutions, body-centered cubic (BCC)/FCC structures were not observed in our study. In fact, none of our samples exhibited such cubic phases, and further increasing the *f* values yielded disordered phases. This likely stems from an ability to maintain uniform shell thickness, which is not observed in BCC or FCC structures due to the uneven spacings between micelles. However, the low symmetry morphology with shape anisotropy developed in this work does exhibit this ability, enabled by fast chain exchange dynamics with high χ value of hydrophobic PMB core and ionic matrices.

Interestingly, when the phase behavior of the same block copolymers in nonionic solvents (i.e., MeOH/DMSO mixtures) was examined, only HEX structures were observed for the PSTFSI-*b*-PMB samples over a wide $f_{PSTFSI} + f_{solvents}$ window. For the case of PSS-*b*-PMB, it was seen that a small portion of the $T - f_{PSS} + f_{solvents}$ phase window was occupied by A15/HEX coexistence,

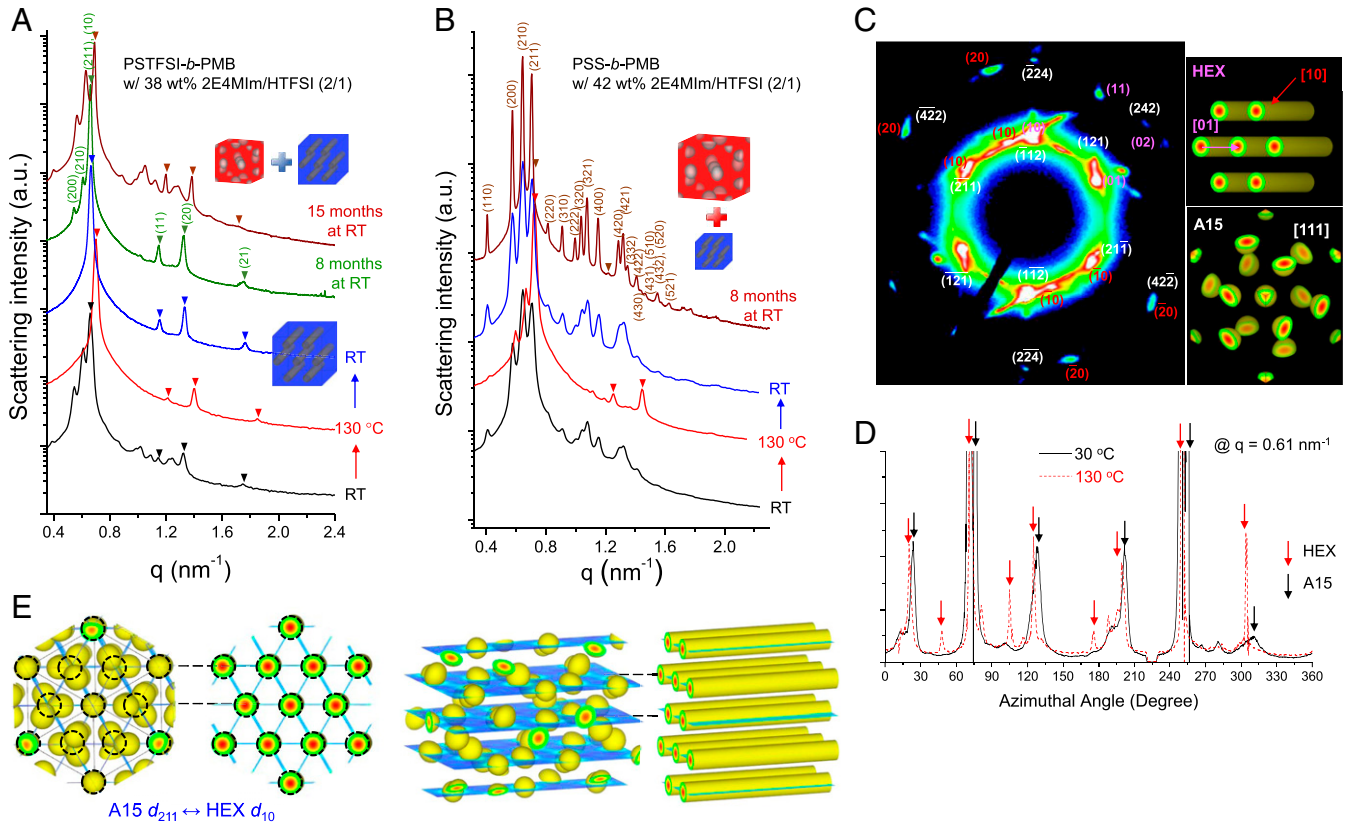

Fig. 2. SAXS profiles of (*A*) PSTFSI-*b*-PMB and (*B*) PSS-*b*-PMB comprising 2E4MIm/HTFSI (2/1) ionic liquids with heating and cooling steps. Bragg peaks corresponding to HEX structures are marked by inverted triangles. (*C*) 2D SAXS pattern of PSS-*b*-PMB comprising 2E4MIm/HTFSI (2/1), representing the coexistence of HEX and A15 crystals. (*D*) Azimuthal scans of the A15 {211} reflection in the 2D scattering patterns at 30 and 130 °C. (*E*) Suggested epitaxial phase route between A15 and HEX structures.

which rapidly transformed into HEX phases upon heating the sample. This indicates that the ionic solvent partitioning exclusively to the charged polymer domains to form thin ionic interfacial layer is a key requirement for expanding the stability window of A15 structures, while the use of nonionic polar solvents rather solvate entire corona chains, analogous to the conventional block copolymer/selective solvent mixtures.

Here, we discuss the epitaxial phase transitions between A15 and HEX structures. As shown in Fig. 2*C*, anisotropic two-dimensional (2D) scattering patterns were obtained for a few samples at room temperature owing to the shear alignment during the loading into SAXS cells. Diffraction patterns could be indexed by coexisting A15 and HEX crystals, specifically, A15 crystals in [111] projection and HEX crystals in [01] and [10] projections with respect to the direction of the incident X-rays. Furthermore, the diffraction pattern of the A15 crystals faded with heating and new peaks corresponding to the HEX structures appeared.

Azimuthal scans of the A15 {211} reflection in the 2D scattering patterns at 30 °C and 130 °C are shown in Fig. 2*D*. The emergence of the {10} reflection in the HEX structures at 19°, 47°, 72°, 104°, 124°, 175°, 199°, 248°, and 304° (red arrows) was noted and is likely a consequence of the A15-to-HEX phase transition that occurs with heating. Interestingly, the new HEX peaks are closely located to those of the original A15 structures (black arrows). This denotes that the A15-to-HEX transition is epitaxial, in which the HEX cylinders are formed by the merging of spheres in the {211} planes of the A15 unit cells. A suggested, epitaxial phase route between the A15 and HEX structures is schematically depicted in Fig. 2*E*. The micelles on the 6c Wyckoff positions of the A15 unit cells could alternatively rearrange in clockwise and counterclockwise fashions, and the merging of those micelles on the {211} planes would yield cylinders on the {10} planes of the HEX structure (49).

Crystallographic Analysis of A15 Structures. When the mass fraction of 2E4MIm/HTFSI (2/1) is increased to 50 wt% or the ratio of 2E4MIm/HTFSI is raised to 3/1, pure A15 structures were observed for both the PSTFSI-*b*-PMB and PSS-*b*-PMB samples regardless of the variation in their thermal treatments. This denotes that the stabilization energy of A15 structures increased with increasing volume fraction of ionic phases or enriched $-SO_3^-$–2E4MIm$^+$ (or –TFSI$^-$–2E4MIm$^+$) interactions in ionic shells. Intriguingly, the experimental form factor analysis of dilute micellar solutions in ionic liquids unveiled a gradual reduction in PMB core size with increasing 2E4MIm content while the thickness of the ionic shells remained intact (*SI Appendix*, Fig. S7 *A* and *B*). This suggests that the increased 2E4MIm/HTFSI ratio increased the micellar curvature to stabilize the low symmetry morphology.

Given that conformational asymmetry has long been used as an important mechanism to rationalize the thermodynamic stability of the A15 phases in miktoarm star polymers (50), we calculated the statistical chain sizes of PMB, PSTFSI, and PSS chains for PSTFSI-*b*-PMB and PSS-*b*-PMB in 2E4MIm/HTFSI by MD simulations (*SI Appendix*, Fig. S7 *C* and *D*). The ratio of statistical chain sizes of PMB to PSS was as large as 1.84, while that of PMB to PSTFSI was as small as 1.68. The value of PSS-*b*-PMB is in good agreement with the literature value of 1.85, reported for A15 phases of neutral diblock copolymer melts (38). Both values exhibited a positive correlation with the number of polymer chains in the micelles. The calculated conformational

asymmetry of dilute micelles in 2E4MIm/HTFSI (1/1) and those constituting A15 phases in 2E4MIm/HTFSI (2/1) were almost identical.

Crystallographic analysis further demonstrates the structural differences between A15 phases with different, tethered acid functional groups. Fig. 3*A* shows representative equilibrium SAXS profiles of PSS-*b*-PMB and PSTFSI-*b*-PMB containing 50 wt% 2E4MIm/TFSI (2/1) that were acquired at room temperature. As indicated by the blue shadow in the figure, the strong scattering intensity of the (110) peak was apparent for PSS-*b*-PMB but was rather indistinct for PSTFSI-*b*-PMB. This was consistently observed for all A15-forming samples, indicative of dissimilar micellar morphologies in A15 phases of PSS-*b*-PMB and PSTFSI-*b*-PMB.

These were visualized by electron density reconstruction using MATLAB and SUPERFLIP software based on structure factors extracted from SAXS profiles and a charge-flipping algorithm (51). Fig. 3*B* delineates the electron density difference isosurface maps and the charge-density contour maps of the A15 unit cells. These maps displayed ellipsoidal-shaped facial micelles in close proximity for both samples, but the aspect ratio was greater in the PSS-*b*-PMB samples. Besides, the distorted shape of the center micelles were visualized for PSTFSI-*b*-PMB owing to the delocalized nature of the $-TFSI^-$ anion, resulting in the soft PSTFSI corona and diffusive micellar interfaces.

Simulated A15 structures of block copolymers in 2E4MIm/HTFSI (2/1) in Fig. 3*C* show striking agreement with the reconstructed electron density map, including more distorted and diffusive micellar interfaces for PSTFSI-*b*-PMB. This distortion is facilitated by fast dynamics of $2E4MIm^+$ cations at the $PSTFSI^-/2E4MIm^+$ interfacial layer, leading to a strong fluctuation of the micelle surface (*SI Appendix*, Fig. S8 and Movie S1). On the contrary, PSS-*b*-PMB shows significantly less fluctuation than that of PSTFSI-*b*-PMB due to the stronger binding of its $PSS^-/2E4MIm^+$ ion pairs in its thin interfacial layer. The contour density map of each species provides valuable insight into the dissimilar interfacial fluctuations and ion distributions (*SI Appendix*, Fig. S9). Particularly, the facial micelles are very closely located to one another as they share $2E4MIm^+$ cations in the thin $PSS^-/2E4MIm^+$ (or $PSTFSI^-/2E4MIm^+$) shell layers. This is enabled by the strong electrostatic interactions that contract the charged polymer chains (*SI Appendix*, Fig. S10). The resultant uniform thickness of the ionic shells allowed the micelles to accommodate the low symmetry morphology.

Enhanced Ionic Conductivity of Charged Block Copolymers by Stabilizing Low Symmetry Morphology. Lastly, we investigated the morphology–transport relationship of our samples. Fig. 4 *A* and *B* show the ionic conductivities of PSTFSI-*b*-PMB and PSS-*b*-PMB comprising 50 wt% ionic liquids with different 2E4MIm/HTFSI ratios. Also of note, the conductivity of the neat ionic liquids is highest at a 1/1 ratio, which gradually decreases as the 2E4MIm content increases (i.e., 1/1 > 3/2 > 2/1 > 3/1, reference *SI Appendix*, Fig. S11*A*). For PSTFSI-*b*-PMB samples, the conductivity was intimately related to the inherent conductivity of the neat ionic liquids, signaling that the 2E4MIm/HTFSI ionic liquids in PSTFSI-*b*-PMB simply act like solvents.

On the contrary, for PSS-*b*-PMB comprising 2E4MIm/HTFSI (1/1), a considerable reduction in ionic conductivity was observed over the entire temperature window of interest. Despite the inferior conductivity of nonstoichiometric 2E4MIm/HTFSI to that of stoichiometric 2E4MIm/HTFSI (in neat states), a radical enhancement in the conductivity by an order of magnitude was seen if the PSS-*b*-PMB samples formed A15 structures with the use of 2E4MIm-excessive ionic liquids. This is attributed to the facilitated proton transport across three-dimensionally connected ionic shells, which are stabilized by electrostatic interactions.

Morphology factors were further quantified based on the Sax–Ottino equation (52). The ionic conductivities of the PSTFSI-*b*-PMB and PSS-*b*-PMB samples were normalized by those of PSS and PSTFSI homopolymer counterparts having the same local concentration of the ionic liquids, that is, the same 2E4MIm/HTFSI ratio (*SI Appendix*, Fig. S11 *B* and *C*). Fig. 4*C* shows the calculated morphology factors of representative sets of the sample, revealing that the highest morphology factor close to unity was for PSTFSI-*b*-PMB with 2E4MIm/HTFSI (1/1), while a markedly low value of less than 0.05 was seen for the PSS-*b*-PMB analog. With embedded 2E4MIm/HTFSI (2/1), both PSTFSI-*b*-PMB and PSS-*b*-PMB formed A15 structures and showed morphology factors in the range of 0.6 to 0.8. The reason the morphology factor is lowered despite having the same A15 structures is due to the enhanced viscosity of 2E4MIm/HTFSI (2/1) when it is confined in ionic phases, making the normalization by homopolymer conductivity imprecise. Yet, it is evident that the morphology of the charged block copolymers played an important role in determining the ion transport efficiency. This is owing to the three-dimensionally connected ionic phases that A15 structures provide, which are unlike

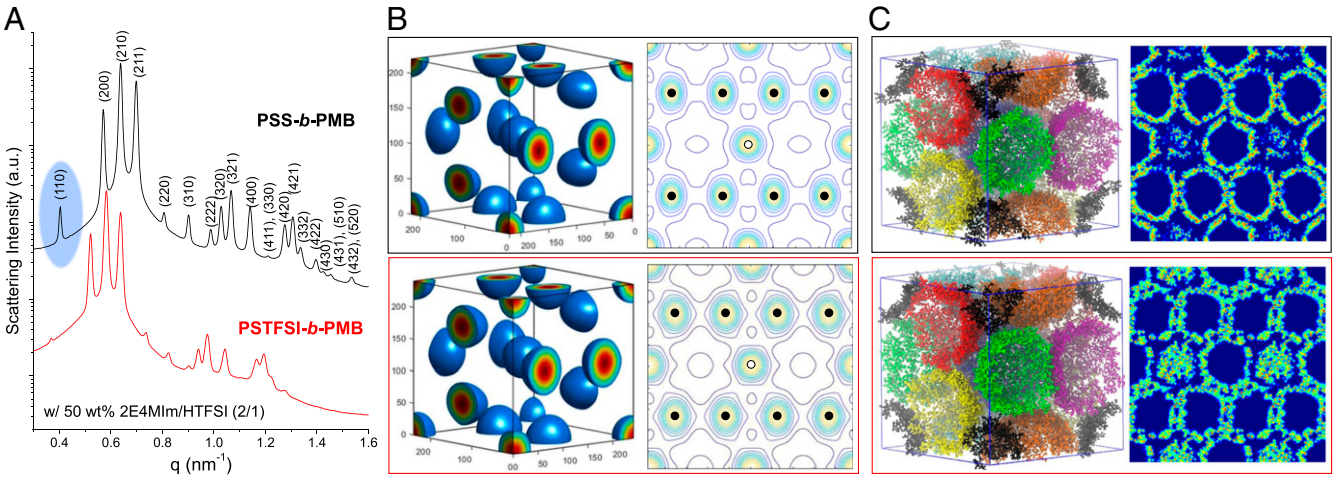

Fig. 3. (*A*) SAXS profiles of PSS-*b*-PMB and PSTFSI-*b*-PMB comprising 50 wt% 2E4MIm/HTFSI (2/1). (*B*) Electron density difference isosurface map and charge-density contour map of each A15 unit cell. (Empty circles are Wyckoff position 2a, and black circles are Wyckoff position 6c.) (*C*) MD simulation snapshot and the contour density map of each A15 structure, drawn for the PSS and PSTFSI chains.

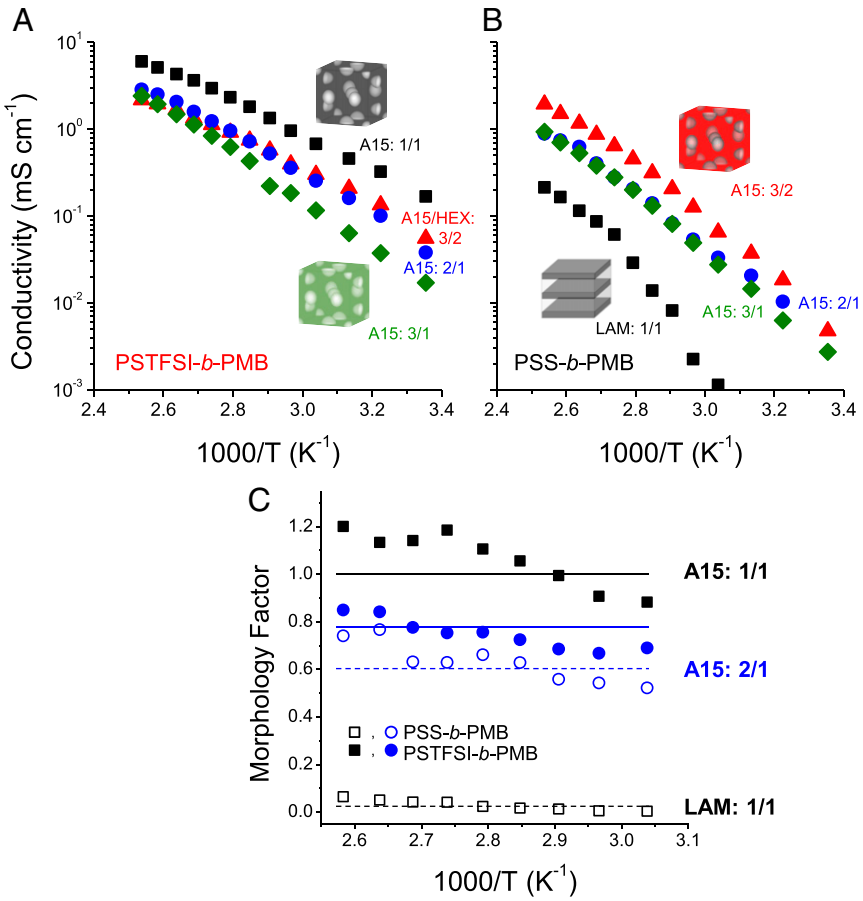

Fig. 4. Temperature-dependent ionic conductivity of (*A*) PSTFSI-*b*-PMB and (*B*) PSS-*b*-PMB comprising 50 wt% 2E4MIm/HTFSI ionic liquids. The molar ratios of 2E4MIm/HTFSI and morphologies of the samples are marked in the figure. (*C*) Morphology factors of representative sets of samples, calculated by Sax–Ottino equation.

the highly tortuous ion-conduction paths formed in LAM structures.

The present study establishes a platform for designing efficient polymer electrolytes via the stabilization of a low symmetry morphology. Therefore, fabricating other Frank–Kasper phases for charged block copolymers may be prudent to pursue in the near future. This could be accomplished via an approach where the molecular size, the strength of electrostatic interactions, the concentration of physically and chemically bound charges, and the block architecture/composition are tuned.

Conclusions

In summary, we investigated the electrostatically controlled morphologies of PSS-*b*-PMB and PSTFSI-*b*-PMB block copolymers. The key findings of this study acquired by combining experiments and computer simulations are summarized as follows: 1) Facile stabilization of A15 phases was unveiled for PSS-*b*-PMB and PSTFSI-*b*-PMB through the incorporation of non-stoichiometric 2E4MIm/HTFSI ionic liquids. 2) PMB micelle cores were predominantly covered with uncharged PS units, followed by the formation of thin ionic shell layers of charged polymer/2E4MIm$^+$ complexes at the interfaces. This played a crucial role in stabilizing the low symmetry morphology of our samples, where the stabilization energy increased with increasing 2E4MIm content. 3) The strong binding of 2E4MIm$^+$ cations to the tethered $-SO_3^-$ groups of PSS-*b*-PMB yielded ellipsoidal facial micelles with sharp interfacial layers, while rather distorted micelles and diffusive micellar interfaces with concentration fluctuations were observed for PSTFSI-*b*-PMB due to its weak binding interactions. 4) The extremely slow reenactment of the A15 structures from HEX phases was noted when the samples were cooled. This was deemed an epitaxial process via the d_{211} of the A15 structures coinciding with the d_{10} of the HEX structures. 5) The development of A15 structures was found to provide efficient ion transport, contrary to a radical reduction in conductivity observed for the LAM-forming samples. Enhancing the ion transport properties of charged block copolymers via interfacial engineering provides a potential route to developing advanced polymer electrolytes.

Materials and Methods

Synthesis of Block Copolymers. The molecular weight and molecular weight distribution of the PS-*b*-PMB precursor block copolymer were 1.1-*b*-1.2 kg · mol^{-1} and 1.05, respectively. Random sulfonation reaction of the PS-*b*-PMB precursor was conducted to have a sulfonation level of 35 mol.%. The PSTFSI-*b*-PMB was synthesized via chlorination and imidazation of the PSS-*b*-PMB.

Morphology Analysis. Morphologies of PS-*b*-PMB and PSTFSI-*b*-PMB block copolymers comprising nonstoichiometric ionic liquids were investigated by Synchrotron SAXS experiments at the Pohang Accelerator Laboratory using the PLS-II 9A and 4C beamlines. A15 structures were visualized by electron density reconstruction using MATLAB and SUPERFLIP software based on structure factors extracted from SAXS profiles and a charge-flipping algorithm.

Ionic Conductivity Measurements. Through-plane ionic conductivities of neat ionic liquids and charged polymer samples were measured by alternating

current impedance spectroscopy (VersaStat3, Princeton Applied Research) in the argon-filled glove box.

MD Simulations. All simulations were performed using OpenMM molecular dynamics package (version 7.4) optimized for massive parallelization with graphical processing unit. Langevin integration scheme with 4 fs time step was used for all systems to constrain the simulations at the desired temperature of 350 K.

More details of the materials, experimental procedures, data, and MD simulations are described in *SI Appendix*.

Data Availability. All study data are included in the article and/or supporting information.

ACKNOWLEDGMENTS. This work was supported by the National Research Foundation of Korea (NRF) grant funded by the Korea government (Ministry of Education, Science and Technology, Grant No. NRF-2017R1A2B3004763) (Ministry of Science and ICT, Grant No. NRF-2017R1A5A1015365). We also acknowledge financial support from the Creative Materials Discovery Program through the NRF funded by Ministry of Science and ICT (2018M3D1A1058624). C.Y.S. acknowledges financial support from NRF (2021R1C1C1009323).

1. L. Leibler, Theory of microphase separation in block copolymers. *Macromolecules* **13**, 1602–1617 (1980).
2. F. H. Schacher, P. A. Rupar, I. Manners, Functional block copolymers: Nanostructured materials with emerging applications. *Angew. Chem. Int. Ed. Engl.* **51**, 7898–7921 (2012).
3. T. P. Lodge *et al*., Structure and dynamics of concentrated solutions of asymmetric block copolymers in slightly selective solvents. *Macromolecules* **29**, 5955–5964 (1996).
4. N. Sakamoto, T. Hashimoto, C. D. Han, D. Kim, N. Y. Vaidya, Effect of addition of a neutral solvent on the order–order and order–disorder transitions in a polystyrene-block-polyisoprene-block-polystyrene copolymer. *Macromolecules* **30**, 5321–5330 (1997).
5. F. S. Bates, G. H. Fredrickson, Block copolymer thermodynamics: Theory and experiment. *Annu. Rev. Phys. Chem.* **41**, 525–557 (1990).
6. T. P. Lodge, B. Pudil, K. J. Hanley, The full phase behavior for block copolymers in solvents of varying selectivity. *Macromolecules* **35**, 4707–4717 (2002).
7. A. A. Teran, N. P. Balsara, Thermodynamics of block copolymers with and without salt. *J. Phys. Chem. B* **118**, 4–17 (2014).
8. D. M. Yu *et al*., Evaluation of the interaction parameter for poly(solketal methacrylate)-block-polystyrene copolymers. *Macromolecules* **51**, 1031–1040 (2018).
9. M. J. Park *et al*., Increased water retention in polymer electrolyte membranes at elevated temperatures assisted by capillary condensation. *Nano Lett.* **7**, 3547–3552 (2007).
10. K. Kempe *et al*., Strongly phase-segregating block copolymers with sub-20 nm features. *ACS Macro Lett.* **2**, 677–682 (2013).
11. E. M. Kolonko, J. K. Pontrello, S. L. Mangold, L. L. Kiessling, General synthetic route to cell-permeable block copolymers via ROMP. *J. Am. Chem. Soc.* **131**, 7327–7333 (2009).
12. A. B. Chang *et al*., Manipulating the ABCs of self-assembly via low-χ block polymer design. *Proc. Natl. Acad. Sci. U.S.A.* **114**, 6462–6467 (2017).
13. H. Y. Jung, S. Y. Kim, O. Kim, M. J. Park, Effect of the protogenic group on the phase behavior and ion transport properties of acid-bearing block copolymers. *Macromolecules* **48**, 6142–6152 (2015).
14. N. Houbenov *et al*., Self-assembled polymeric supramolecular frameworks. *Angew. Chem. Int. Ed. Engl.* **50**, 2516–2520 (2011).
15. J. D. Cushen *et al*., Thin film self-assembly of poly(trimethylsilylstyrene-b-d,l-lactide) with sub-10 nm domains. *Macromolecules* **45**, 8722–8728 (2012).
16. Y. Hibi *et al*., Self-template-assisted micro-phase segregation in blended liquid-crystalline block copolymers films toward three-dimensional structures. *Proc. Natl. Acad. Sci. U.S.A.* **117**, 21070–21078 (2020).
17. H. S. Kang *et al*., Printable and rewritable full block copolymer structural color. *Adv. Mater.* **29**, 1700084 (2017).
18. S. Y. Kim, S. Kim, M. J. Park, Enhanced proton transport in nanostructured polymer electrolyte/ionic liquid membranes under water-free conditions. *Nat. Commun.* **1**, 88 (2010).
19. R. Bouchet *et al*., Single-ion BAB triblock copolymers as highly efficient electrolytes for lithium-metal batteries. *Nat. Mater.* **12**, 452–457 (2013).
20. O. Kim, H. Kim, U. H. Choi, M. J. Park, One-volt-driven superfast polymer actuators based on single-ion conductors. *Nat. Commun.* **7**, 13576 (2016).
21. T. Ito, G. Ghimire, Electrochemical applications of microphase-separated block copolymer thin films. *ChemElectroChem* **5**, 2937–2953 (2018).
22. O. Kim, K. Kim, U. H. Choi, M. J. Park, Tuning anhydrous proton conduction in single-ion polymers by crystalline ion channels. *Nat. Commun.* **9**, 5029 (2018).
23. J. Shim, F. S. Bates, T. P. Lodge, Superlattice by charged block copolymer self-assembly. *Nat. Commun.* **10**, 2108 (2019).
24. O. Kim *et al*., Phase behavior and conductivity of sulfonated block copolymers containing heterocyclic diazole-based ionic liquids. *Macromolecules* **45**, 8702–8713 (2012).
25. J. Jiang, X. Chen, S. Yang, E.-Q. Chen, The size and affinity effect of counterions on self-assembly of charged block copolymers. *J. Chem. Phys.* **152**, 124901 (2020).
26. C. E. Sing, J. W. Zwanikken, M. Olvera de la Cruz, Electrostatic control of block copolymer morphology. *Nat. Mater.* **13**, 694–698 (2014).
27. C. E. Sing, J. W. Zwanikken, M. Olvera de la Cruz, Theory of melt polyelectrolyte blends and block copolymers: Phase behavior, surface tension, and microphase periodicity. *J. Chem. Phys.* **142**, 034902 (2015).
28. V. A. Pryamitsyn, H.-K. Kwon, J. W. Zwanikken, M. Olvera de la Cruz, Anomalous phase behavior of ionic polymer blends and ionic copolymers. *Macromolecules* **50**, 5194–5207 (2017).
29. M. J. Park, N. P. Balsara, Phase behavior of symmetric sulfonated block copolymers. *Macromolecules* **41**, 3678–3687 (2008).
30. H. Y. Jung, O. Kim, M. J. Park, Ion transport in nanostructured phosphonated block copolymers containing ionic liquids. *Macromol. Rapid Commun.* **37**, 1116–1123 (2016).
31. O. Kim, S. Y. Kim, J. Lee, M. J. Park, Building less tortuous ion-conduction pathways using block copolymer electrolytes with a well-defined cubic symmetry. *Chem. Mater.* **28**, 318–325 (2016).
32. H. Y. Jung, M. J. Park, Thermodynamics and phase behavior of acid-tethered block copolymers with ionic liquids. *Soft Matter* **13**, 250–257 (2016).
33. N. Xie, W. Li, F. Qiu, A.-C. Shi, σ Phase formed in conformationally asymmetric AB-type block copolymers. *ACS Macro Lett.* **3**, 906–910 (2014).
34. M. Liu, W. Li, F. Qiu, A.-C. Shi, Stability of the Frank-Kasper σ-phase in BABC linear tetrablock terpolymers. *Soft Matter* **12**, 6412–6421 (2016).
35. M. W. Schulze *et al*., Conformational asymmetry and quasicrystal approximants in linear diblock copolymers. *Phys. Rev. Lett.* **118**, 207801 (2017).
36. A. Reddy *et al*., Stable Frank-Kasper phases of self-assembled, soft matter spheres. *Proc. Natl. Acad. Sci. U.S.A.* **115**, 10233–10238 (2018).
37. A. J. Mueller *et al*., Quasicrystals and their approximants in a crystalline–amorphous diblock copolymer. *Macromolecules* **54**, 2647–2660 (2021).
38. M. W. Bates *et al*., Stability of the A15 phase in diblock copolymer melts. *Proc. Natl. Acad. Sci. U.S.A.* **116**, 13194–13199 (2019).
39. S. Jeon *et al*., Frank–Kasper phases identified in PDMS-b-PTFEA copolymers with high conformational asymmetry. *Macromol. Rapid Commun.* **40**, e1900259 (2019).
40. H. Takagi, K. Yamamoto, Phase boundary of Frank–Kasper σ phase in phase diagrams of binary mixtures of block copolymers and homopolymers. *Macromolecules* **52**, 2007–2014 (2019).
41. A. J. Mueller *et al*., Emergence of a C15 Laves phase in diblock polymer/homopolymer blends. *ACS Macro Lett.* **9**, 576–582 (2020).
42. S. Xie, A. P. Lindsay, F. S. Bates, T. P. Lodge, Formation of a C15 Laves phase with a giant unit cell in salt-doped A/B/AB ternary polymer blends. *ACS Nano* **14**, 13754–13764 (2020).
43. A. P. Lindsay *et al*., A15, σ, and a quasicrystal: Access to complex particle packings via bidisperse diblock copolymer blends. *ACS Macro Lett.* **9**, 197–203 (2020).
44. M. Liu, Y. Qiang, W. Li, F. Qiu, A.-C. Shi, Stabilizing the Frank-Kasper phases via binary blends of AB diblock Copolymers. *ACS Macro Lett.* **5**, 1167–1171 (2016).
45. A. Jayaraman, D. Y. Zhang, B. L. Dewing, M. K. Mahanthappa, Path-dependent preparation of complex micelle packings of a hydrated diblock oligomer. *ACS Cent. Sci.* **5**, 619–628 (2019).
46. B. Kim, H. Kang, K. Kim, R.-Y. Wang, M. J. Park, All-solid-state lithium–organic batteries comprising single-ion polymer nanoparticle electrolytes. *ChemSusChem* **13**, 2271–2279 (2020).
47. C. Y. Son, J. G. McDaniel, J. R. Schmidt, Q. Cui, A. Yethiraj, First-principles united atom force field for the ionic liquid BMIM+BF4–: An alternative to charge scaling. *J. Phys. Chem. B* **120**, 3560–3568 (2016).
48. C. Y. Son, J. G. McDaniel, Q. Cui, A. Yethiraj, Conformational and dynamic properties of poly(ethylene oxide) in BMIM+BF4–: A microsecond computer simulation study using ab initio force fields. *Macromolecules* **51**, 5336–5345 (2018).
49. K. K. Lachmayr, C. M. Wentz, L. R. Sita, An exceptionally stable and scalable sugar–polyolefin Frank–Kasper A15 phase. *Angew. Chem. Int. Ed. Engl.* **59**, 1521–1526 (2020).
50. G. M. Grason, R. D. Kamien, Interfaces in diblocks: A study of miktoarm star copolymers. *Macromolecules* **37**, 7371–7380 (2004).
51. Z. Jiang, B. Lee, Recent advances in small angle X-ray scattering for superlattice study. *Appl. Phys. Rev.* **8**, 011305 (2021).
52. J. Sax, J. M. Ottino, Modeling of transport of small molecules in polymer blends: Application of effective medium theory. *Polym. Eng. Sci.* **23**, 165–176 (1983).